(Received 28 February 2026, Accepted 3 April 2026, Scheduled 20 April 2026)

Nested-Level Optimization of a Permanent Magnet Synchronous Motor Embedded in Energy Management for Hybrid Electric Vehicles

Zhijia Jin[1], Cong Liang[2,*], Xin Lu[1], and Jian Chen[1]

[1] *School of Automotive Engineering, Suzhou University of Technology, Changshu, China*
[2] *Automotive Engineering Research Institute, Jiangsu University, Zhenjiang, China*

ABSTRACT: In addition to considering the electromagnetic performance of the motor itself, the optimal design of an onboard permanent magnet synchronous motor (PMSM) must also account for its compatibility with a vehicle and the impact of driving cycles. To address this problem, in this study, we propose a nested optimization design approach for PMSMs to achieve an optimal rotor design for vehicular applications. First, Morris sensitivity analysis is employed to classify the parameters to be optimized into highly and generally sensitive parameters. Subsequently, the Kriging model and NSGA-III algorithm are successively applied to perform hierarchical optimization for the highly sensitive parameters, followed by the generally sensitive parameters. To select the motor structure that best adapts to the vehicle and driving cycle, the efficiency maps of candidate solutions are solved and nested into the vehicle energy management model for optimization. The results demonstrate that the proposed method enables the identification of PMSM structures on the Pareto front that better match the vehicle and driving cycle. Compared with other high-performance solutions, the final optimal point achieves fuel consumption savings of up to 19.1%.

1. INTRODUCTION

Permanent magnet synchronous motors (PMSMs), prized for their high power density and high electromagnetic torque, have become a preferred drive solution for new energy vehicles, particularly in hybrid electric vehicles (HEVs) [1–4]. Consequently, enhancing the electromagnetic performance of PMSMs for HEVs has become a major focus of research and development.

The optimization design of the PMSM structure is a crucial approach to enhancing its output performance. Due to the nonlinear problem, an extremely accurate PMSM mathematical model is hard to establish [5]. Hence, the finite element analysis (FEA) method is a widely accepted alternative solution. With the rapid development of computational capabilities, a significant number of studies have been conducted using FEA. In [6], FEA simulates air-gap flux density harmonics, torque ripple, and radial air-gap electromagnetic force density, providing data for Kriging surrogate model-based two-step optimization. With the help of FEA, the optimization model enables a 4.2% main operating points efficiency rise and sharp reduction in 3rd/5th/7th harmonics, lower torque ripple, and air-gap electromagnetic force density. Ref. [7] developed analytical models to efficiently optimize winding loss in a special flexible printed circuit board hexagonal slotless PMSM. FEA was used solely to validate the accuracy of the proposed analytical models for eddy current loss, circulating current loss, and electromagnetic torque. While the above studies utilized FEA for PMSM optimization, a significant challenge is frequently mentioned: the substantial computational cost. For example, consider an electromagnetic device defined by eight design parameters. A full design with 5 levels for each parameter would necessitate 390,625 FEA calculations, which is computationally prohibitive.

To solve the computational problem in high-dimensional optimization design, various optimization methods have been proposed. There are two typical types of solutions. One is the sensitivity analysis [8, 9], and the other is the surrogate model [10, 11]. In [12], a lumped unit force response-based multiphysics sensitivity analysis was adopted, which quantified parameter impacts on electromagnetic-structural performance, the key parameters and revealed tradeoffs to underpin NVH were accurately identified. Pearson correlation coefficient was proposed to quantify parameter-objective correlations and classify parameters into subspaces. The results demonstrate that this method cuts computational cost for the multilevel optimization of PMSM drive systems in [13]. Furthermore, sensitivity analysis methods such as analysis of variance, the Morris method, and the Kendall correlation coefficient have also been proposed to screen parameters for optimization, thereby reducing simulation time. As for surrogate models, response surface methodology [14], Kriging model [15], artificial neural networks [16], and Bayesian optimization [17] are widely used in the PMSM optimization. Ref. [18] proposed a Kriging-assisted surrogate model to replace FEA during optimization, achieving time saving and high prediction accuracy simultaneously. Ref. [19] fitted the regression equations of the significant

* Corresponding author: Cong Liang (cong@ujs.edu.cn).

variables and optimization objectives by the response surface method. The cross-validation percentage results indicated high model accuracy with the maximum error only 5.44%. Thanks to the development of artificial intelligence in recent years, surrogate models, including artificial neural networks, have seen a certain level of application. In [20], an automatic design system with a deep generative model and a convolutional neural network was proposed to generate a large amount of data from a small number of FEA results. The system was successfully applied to multi-objective optimization design with very little time.

In addition to the issues related to electromagnetic optimization, another problem with PMSM is its adaptability when used in HEVs. In HEVs, the performance of the energy management strategy is determined by the motor outputs, including instantaneous efficiency and maximum torque, which subsequently influence the overall operational cost of the vehicle. Thus, it is essential to account for the operational environment, namely, the torque distribution strategy and energy flow path during the optimization of the MSM used in HEVs [21]. Co-optimized powertrain parameters, including motor sizes and ECMS-based energy management for HEV, achieved major fuel savings and component reductions. In [22], a hybrid NSGA-II and deep reinforcement learning framework was proposed. This framework co-optimized the electric motor size and energy management system parameters, simultaneously minimizing fuel consumption and component aging across various driving cycles. In addition, the motor parameters were adjusted while precisely modeling its efficiency map, and co-optimized with other HEV components to elevate motor operation efficiency and overall fuel economy in [23]. Therefore, the co-optimization of motor design and vehicle-level control strategy is proven essential by the aforementioned studies.

Based on the analysis of the current research, it can be found that existing optimization studies on hybrid systems are primarily limited to individual components, often focusing solely on energy management strategy design or the optimization of engines and motors, while lacking a system-level optimization approach that coordinates all components. In addition, motor optimization faces challenges such as a large number of parameters, strong nonlinearities, and high computational costs. To improve both the motor output performance and vehicle fuel economy, in this study, a nested-level optimization for the PMSM rotor and energy management strategy parameters is proposed. The main contributions of this paper are as follows:

1) Different from the separate optimization of motor parameters or energy management parameters, this paper proposes a nested optimization framework that performs system-level optimization of both motor structural parameters and energy management parameters to improve the driving economy of HEVs.

2) In the optimization process, sensitivity analysis using the Morris method, the Kriging surrogate model, and the NSGA-III optimization algorithm are employed, which significantly reduce the computational cost of the simulation.

The remainder of this paper is structured as follows. In Section 2, the architecture of the HEV, the topology of the PMSM, and the energy management strategy are introduced. Section 3 illustrates the main nested level optimization process, including the Morris method sensitivity analysis, Kriging model and NSGA-III algorithm. The optimization results and discussions are presented in Section 4, followed by the conclusion in Section 5.

2. STRUCTURE AND CONTROL STRATEGY

2.1. PHEV Architecture and Motor Topology

Figure 1 shows the architecture of the PHEV, which is equipped with a coaxial parallel powertrain. The powertrain mainly includes an engine, an automated mechanical transmission (AMT), an interior PMSM, and a power battery. As shown in Fig. 1, the engine and PMSM are mounted on the same output shaft. Their outputs are combined through the transmission assembly and then delivered to the wheels. Under such an architecture, the PMSM can optimize the engine operating points and enhance the overall efficiency. At the same time, the low-speed high-torque characteristic of the PMSM directly compensates for the insufficient low-speed torque of the engine, solving the problem of weak climbing ability in the traditional system. Therefore, the optimization of the motor not only has a significant impact on its own performance but also affects the fuel economy of the Plug-in Hybrid Electric Vehicle (PHEV). The simplified topology of the PMSM applied in the PHEV is shown in Fig. 2. It is a three-phase, eight-pole, 48-slot interior PMSM.

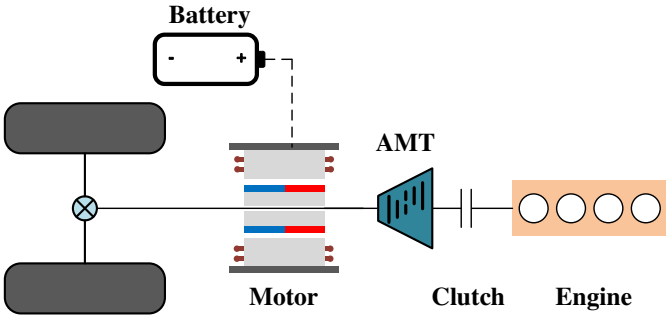

FIGURE 1. Architecture of the PHEV.

2.2. Energy Management Strategy

As a typical strategy applicable to instantaneous energy management strategies, the Equivalent Consumption Minimization Strategy (ECMS) was employed for vehicle torque distribution in this study. The principle of the ECMS is to convert the vehicle's electrical energy consumption into equivalent fuel consumption, with the aim of minimizing the instantaneous equivalent fuel consumption by allocating torque between the engine and electric motor. The instantaneous equivalent fuel consumption can be calculated as follows:

$$\dot{m}_{f,eqv}(t) = \dot{m}_f(t) + \dot{m}_{ress}(t) \quad (1)$$

$$\dot{m}_{ress}(t) = \frac{s(t)}{Q_{lhv}} P_b(t) \quad (2)$$

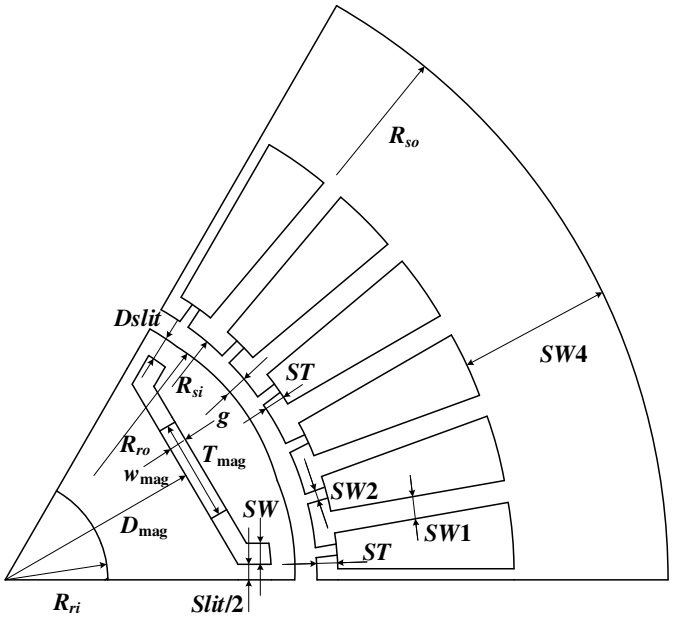

FIGURE 2. Topology of PMSM.

where s is the equivalent factor (EF); Q_{lhv} is the fuel low calorific value; P_b is the battery power; $\dot{m}_{f,}(t)$ and $\dot{m}_{ress}(t)$ represent instantaneous fuel consumption and the electricity equivalent fuel consumption, respectively.

The battery power can be mathematically represented in the motor demand formula as

$$P_b(t) = \frac{T_m \omega_m}{9550 \eta_b \eta_t} \tag{3}$$

where T_m is the motor torque; ω_m is the motor speed; η_b and η_t are the battery and motor efficiencies, respectively. Note that in the process of energy distribution, motor efficiency directly affects the selection of motor torque, which once again demonstrates the necessity of optimization.

3. NESTED-LEVEL OPTIMIZATION

In the case of PMSMs applied in HEVs, the performance of the motor significantly influences the energy management strategy. Therefore, in this study, a nested-level optimization framework is proposed to simultaneously optimize the motor design and the parameters of the energy management strategy.

3.1. Morris Method

The core advantages of the Morris method are mainly reflected in three aspects: Firstly, the computational cost is extremely low, enabling the evaluation of all parameters with a relatively small number of model runs; secondly, as a global method, it avoids the potential misjudgment caused by traditional local sensitivity analysis (such as calculating partial derivatives) in nonlinear models; thirdly, by providing the standard deviation indicator, it can effectively identify whether there are strong interactions between parameters. For the optimization of permanent magnet synchronous motors, which have a large number of parameters, strong nonlinearity, and uncertain interactions between parameters, the Morris method is highly suitable for sensitivity analysis. The Morris method employs probabilistic uniform sampling to estimate the importance of each input factor on the model output. It computes a sensitivity measure for each parameter by systematically varying its value across the defined space and comparing the resulting changes in the output. Specifically, the method calculates elementary effects for each parameter to quantify global influence. The calculation of the elementary effect can be expressed as

$$EE_i = \frac{f(x_1, x_2, \ldots, x_i + \Delta_i, \ldots x_m) - f(x)}{\Delta_i} \tag{4}$$

Subsequently, the global influence of each parameter on the model output can be calculated as follows:

$$\mu_i = \frac{1}{r} \sum_{j=1}^{r} EE_i^j \tag{5}$$

where μ_i is the mean of the elementary effect, and r represents the sampling size.

In this specific process, the Morris method performs systematic random perturbations on the input variables while monitoring the output changes. It then ranks and categorizes the variables based on both the mean change and the variability induced by each.

3.2. Kriging Model

Kriging is a statistical modeling method for optimal spatial interpolation that inherently provides a measure of prediction uncertainty. Generally, the Kriging model can be expressed as

$$Y(x) = \mu + Z(x) \tag{6}$$

where μ is an unknown constant, and $Z(x)$ is a stationary Gaussian stochastic process with zero mean. The covariance of the $Z(x)$ is

$$Cov\left[Z\left(x^{(i)}\right), Z\left(x^{(j)}\right)\right] = \sigma^2 R\left(x^{(i)}, x^{(j)}; \theta\right) \tag{7}$$

where σ is the process variance, θ the correlation length parameters, and R the correlation function, which can be expressed as follows:

$$R\left(x^{(i)}, x^{(j)}; \theta\right) = \exp\left(-\sum_{k=1}^{d} \theta_k \left(x_k^{(i)} - x_k^{(j)}\right)^2\right) \tag{8}$$

Given n sample points $\mathbf{X}$ and their corresponding responses $\mathbf{y}$, for a new point x^*, the prediction $\hat{y}$ and its mean squared error can be expressed as follows:

$$\hat{y}(x^*) = \hat{\mu} + \mathbf{r}\left(x^*\right)^T \mathbf{R}^{-1}\left(y - \mathbf{1}_{(n\times 1)}\hat{\mu}\right) \tag{9}$$

$$s^2(x^*) = \hat{\sigma}^2\left[1 - \mathbf{r}(x^*)^T \mathbf{R}^{-1} r(x^*) + \frac{\left(1 - \mathbf{1}_{(n\times 1)}^T \mathbf{R}^{-1} \mathbf{r}\left(x^*\right)\right)^2}{\mathbf{1}_{(n\times 1)}^T \mathbf{R}^{-1} \mathbf{1}_{(n\times 1)}}\right] \tag{10}$$

where $\mathbf{R}$ is the $n \times n$ correlation matrix, and $\mathbf{r}$ is the correlation vector between x^* and the sample points.

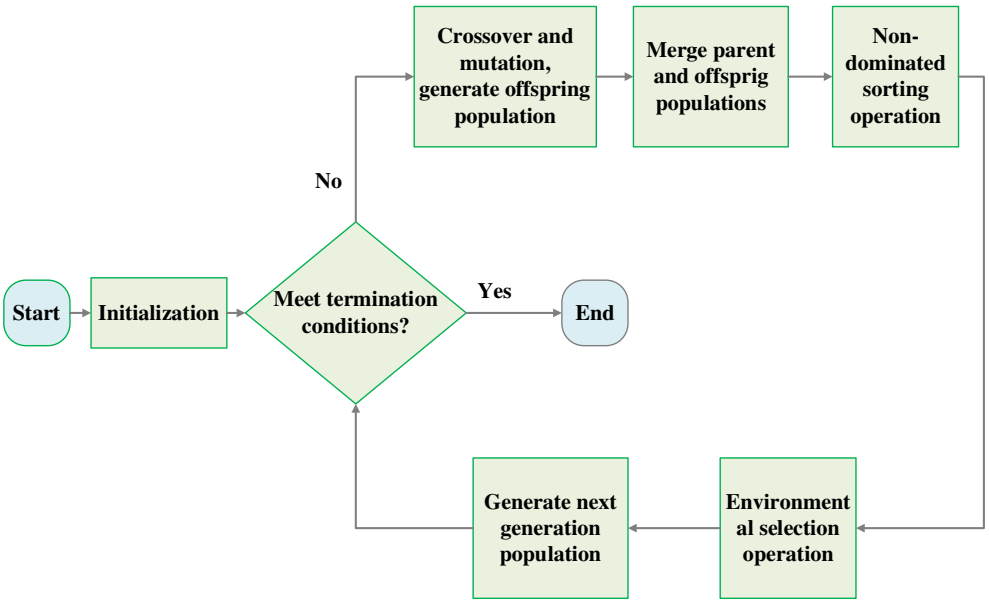

FIGURE 3. The flowchart of the NSGA-III algorithm.

3.3. NSGA-III Algorithm

In this study, the NSGA-III algorithm was used for motor optimization. The algorithm flow is shown in Fig. 3, which includes population initialization, crossover, mutation, and offspring generation, merging parent and offspring populations, non-dominated sorting, environmental selection, and next-generation population generation.

The main framework of NSGA-III is similar to that of NSGA-II, with the primary difference in the environmental selection step. The environmental selection step can be divided into three parts: reference point determination and association, adaptive normalization of the population and niche-preservation operation.

Generally, the reference points are generated using the Das and Dennis method. The total number of reference points can be determined using the combinatorial formula C ($M + p - 1$, p), where M is the number of objectives, and p is the number of divisions along each objective axis. Subsequently, each population member is associated with the direction of the nearest reference point.

The adaptive normalization process begins by computing the minimum of each objective and shifting all objective values accordingly. It then identifies extreme points that define the boundaries of the current frontier and uses them to construct a hyperplane, from which the intercepts for each objective are derived. Finally, normalization is achieved by dividing the shifted objective values by their respective intercepts.

The core of the niche-preservation operation is the use of niche counts. During selection, the reference directions with the fewest associated solutions are consistently prioritized. Within each such direction, the solution with the best convergence is chosen.

3.4. Optimization Architecture

Figure 4 shows a complete nested-level optimization flowchart that specifically includes four steps: initialization, sensitivity analysis, nested optimization, and performance evaluation.

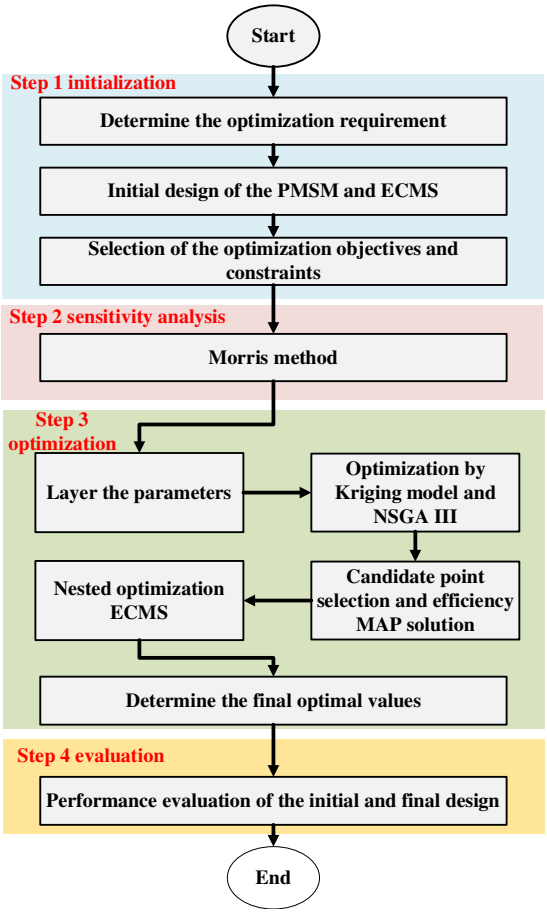

FIGURE 4. Flowchart of the nested-level optimization.

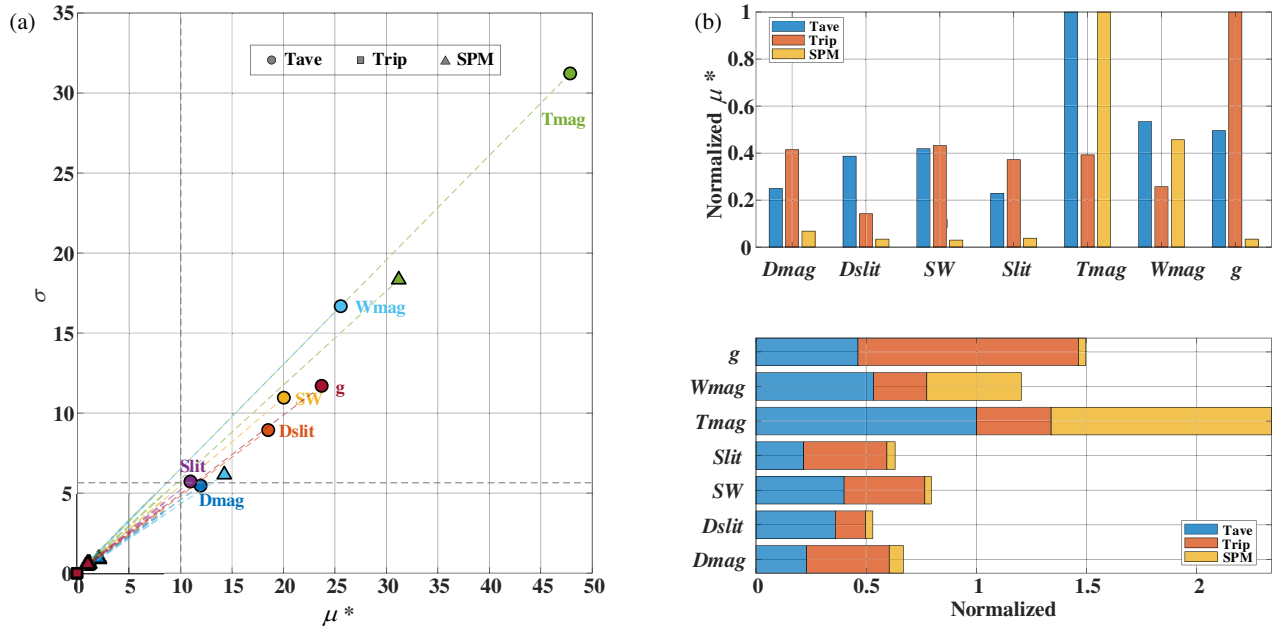

FIGURE 5. The results of Morris sensitivity analysis. (a) Morris sensitivity analysis. (b) Normalized results.

In conventional PMSM optimization, the typical objectives include electromagnetic torque, torque ripple, and motor cost, among others. The optimization objectives can be expressed as

$$\min: \begin{cases} -\text{Tave} = -T_{\max}(x_1, x_2, \ldots, x_n) \\ \text{SPM} = P_c(x_1, x_2, \ldots, x_n) \\ \text{Trip} = R_p(x_1, x_2, \ldots, x_n) \end{cases} \tag{11}$$

$$s.t. \begin{cases} P_c(x_1, x_2, \ldots, x_n) \le P_{need} \\ T_{\max}(x_1, x_2, \ldots, x_n) \ge T_{need} \\ R_p(x_1, x_2, \ldots, x_n) \le R_{need} \end{cases} \tag{12}$$

where $T_{\max}$ is the maximum torque, P_c the cost, R_p the torque ripple, and x_i the parameters to be optimized.

In terms of the energy management strategy, the optimization objective for the control parameters is to minimize the cost of operational energy losses, that is,

$$\min: \int \dot{m}_{f,eqv}(s_1, s_2, \ldots, s_n; t)\, dt \tag{13}$$

where s_i denotes the control parameters to be optimized.

Combining (11)–(13) and the constraints in the HEV, the complete nested-level optimization model can be expressed as

$$\min: \int \dot{m}_{f,eqv}(s_1, s_2, \ldots, s_n, x_1, x_2, \ldots, x_n; t)\, dt \tag{14}$$

$$s.t. \begin{cases} P_c(x_1, x_2, \ldots, x_n) \le P_{need} \\ T_{m\max}(x_1, x_2, \ldots, x_n) \ge T_{need} \\ R_p(x_1, x_2, \ldots, x_n) \le R_{need} \\ soc_l \le soc \le soc_h \\ T_{e\min} \le T_e \le T_{e\max} \\ T_{m\min} \le T_m \le T_{m\max} \\ \omega_{\min} \le \omega_{\min} \le \omega_{\max} \end{cases} \tag{15}$$

After the objectives and constraints were determined, the Morris method was adopted to distinguish between sensitive and non-sensitive variables. Subsequently, Kriging model was established to approximately estimate the performance space. Afterwards, the NSGA-III algorithm was used to solve the Pareto optimal set, and the feasible solutions from the Pareto-optimal set were nested into the energy management model to determine the ultimate optimal solution. Finally, an evaluation step was proposed to assess the quality of the performance.

4. RESULTS AND ANALYSIS

4.1. Results of the Motor Level

In this study, the rotor of the PMSM was optimized, and the main dimensional parameters and their ranges are listed in Table 1.

TABLE 1. Main dimension parameters of the rotor.

Symbol	Parameters	Ranges
Dmag	Magnet inner radius/mm	36–40
Dslit	Flux bridge thickness/mm	1–2
SW	Flux barrier width/mm	2–4
Slit	Interpole flux barrier width/mm	2–4
Tmag	Magnet thickness/mm	2–4
Wmag	Magnet width/mm	17–22
g	Air gap length/mm	0.8–1.5

Figure 5(a) illustrates the results of the Morris sensitivity analysis, where the x-axis represents the absolute mean of the elementary effects μ^*, indicating the overall influence of each parameter on the objectives, and the y-axis represents the standard deviation σ, reflecting the nonlinear effects associated with each parameter. The dashed lines (dotted lines in Fig. 5(a))

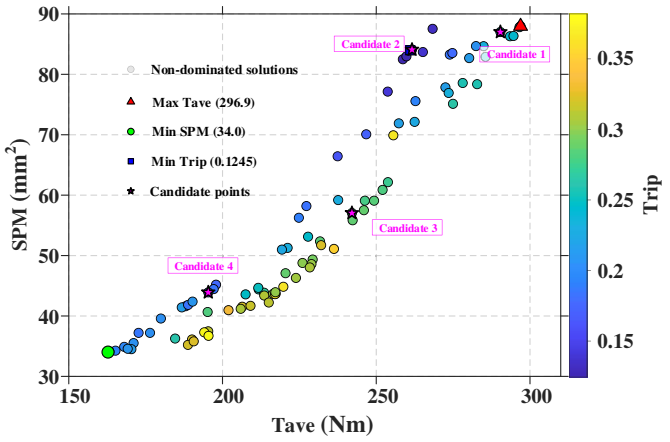

FIGURE 6. Pareto front of the L1 optimization.

divide the μ^*-σ plane into four quadrants, and sensitive parameters are usually located in the upper right quadrant. As shown, *Tmag* has the largest absolute mean value of 47.85 and the largest standard deviation of 31.22 for Tave, and it also shows high values for the surface permanent magnet (SPM) objective. Therefore, *Tmag* is selected as a highly sensitive parameter in this optimization. Additionally, the *g* and *Wmag* also exhibit a relatively high influence on Tave and are consequently classified as highly sensitive parameters. The remaining parameters, *Dslit*, *SW*, *Slit*, and *Dmag*, are categorized as generally sensitive parameters. To facilitate a more intuitive analysis, the normalized results are presented in Fig. 5(b).

Figure 6 shows the Pareto curve of Level I optimization with highly sensitive parameters. The maximum torque can reach 296.9 Nm, the minimum ripple is 12.45% and the minimum magnet area is 34 mm^2. On the Pareto front, points with high torque are accompanied by a large magnet area, whereas points with low torque ripple are distributed in regions of large magnet area and low torque. Candidate points were selected from each region to proceed with the next optimization, as shown in Fig. 6. The optimization results for the candidates are listed in Table 2.

TABLE 2. Results of the level I optimization.

Point	*g* mm	*Tmag* mm	*Wmag* mm	Tave Nm	SPM mm^2	Trip
1	0.85	4.00	21.77	290.37	87.00	0.23
2	1.49	4.00	21.03	261.62	84.09	0.13
3	0.91	2.59	21.99	242.08	57.05	0.28
4	1.50	2.01	21.81	195.36	43.91	0.18

Note that, after completing level I optimization, there are no parameters related to SPM remaining in the parameters to be optimized. Therefore, in level II optimization, it is merely a two-objective optimization of torque and ripple. Fig. 7 shows the Pareto curves in level II optimization, where Figs. 7(a)–(d) correspond to the four candidate points in level I, respectively. Generally, the torque and ripple of the solutions on all four Pareto curves are superior to those of the candidate points. In addition, after the highly sensitive parameters are determined, the ranges of target changes in level II also become smaller. Because the improvement in the optimization objective is relatively small, the final optimization point at level II is no longer selected from individual regions; instead, only the solution from the central region is adopted as the final solution.

The optimization results for level II are listed in Table 3. Although high-performance solutions are ultimately obtained through multilevel motor optimization, it remains impossible to determine which of these solutions is more reasonable. Therefore, in this study, the final motor is selected by conducting a nested optimization in conjunction with HEV energy management. Therefore, the efficiency maps of the solutions in Table 3 are solved and shown in Fig. 8. In these motor efficiency maps, the 50% efficiency contour and external characteristic boundary are presented. The peak efficiency regions are all approximately 96%, but there are certain differences in the corresponding speed ranges in which these peak efficiency regions occur. The discrepancies in the peak efficiency zone and other high-efficiency intervals influence the matching characteristics between the vehicle and its driving cycles, ultimately resulting in variations in the operating economy.

TABLE 3. Results of the level II optimization.

Point	*Dmag* mm	*Dslit* mm	*SW* mm	*Slit* mm	Tave Nm	Trip
L2-1	40.00	1.36	3.85	4.00	325.50	0.12
L2-2	40.00	1.57	3.31	3.99	279.96	0.08
L2-3	39.92	1.26	4.00	4.00	273.46	0.15
L2-4	39.99	1.24	4.00	4.00	219.48	0.12

4.2. Results of the Nested Level

In this study, nested optimization considers the compatibility of the motor with a vehicle and driving cycle. The selected driving cycle is the commonly used passenger car test cycle, CLTC-P, which features low-, medium-, and high-speed phases representing typical urban and suburban driving conditions in China, as shown in Fig. 9. Based on the characteristics of CLTC-P, distinct EFs are assigned to the low-, medium-, and high-speed regions. Furthermore, the driving cycle is run thrice in each simulation, resulting in a total of nine EF variables to be optimized. In addition, the vehicle parameters are listed in Table 4.

TABLE 4. Parameters of the vehicle.

Parameters	Value
Vehicle mass/kg	1400
Frontal area/m^2	1.75
Tire radius/m	0.287
Rolling resistance coefficient	0.008
Aerodynamic drag coefficient	0.3
Peak power of engine/kW	62
Battery capacity/Ah	120

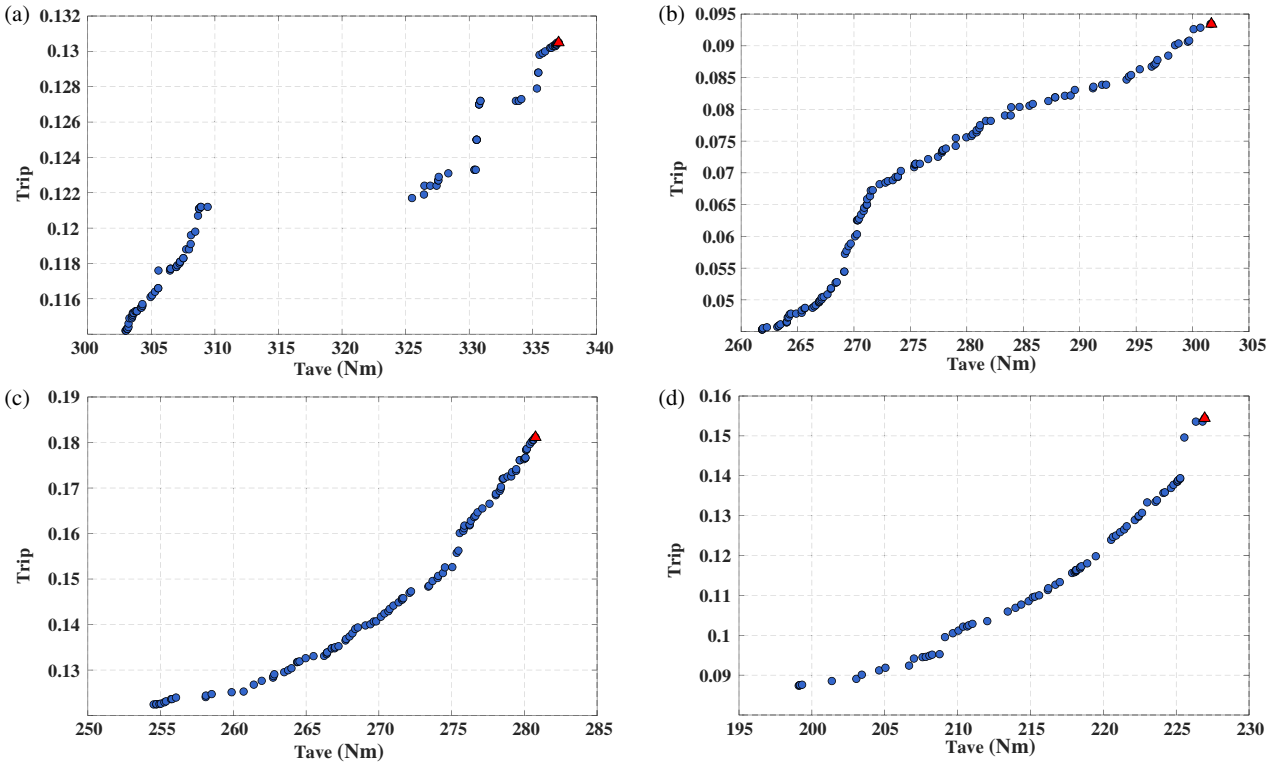

FIGURE 7. Pareto front of the L2 optimization. (a) Pareto Front L2-1. (b) Pareto Front L2-2. (c) Pareto Front L2-3. (d) Pareto Front L2-4.

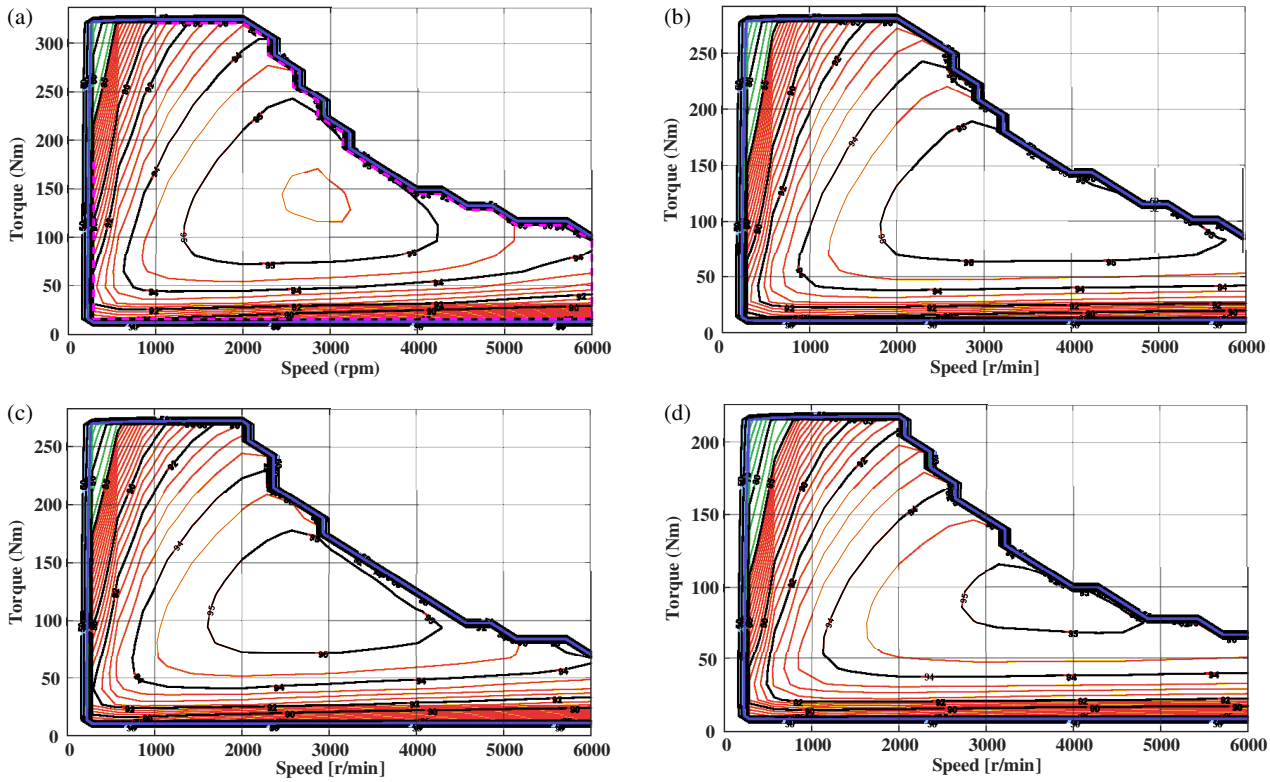

FIGURE 8. Efficiency maps of the candidates. (a) L2-1. (b) L2-2. (c) L2-3. (d) L2-4.

The results of the nested-level optimization are shown in Figs. 10 and 11. As shown, the value of EF directly determines the output of the electric motor. When the EF value is relatively large, the motor output tends to be lower, resulting in a rapid increase in fuel consumption. Owing to differences in the maximum torque and efficiency of the motors, the selec-

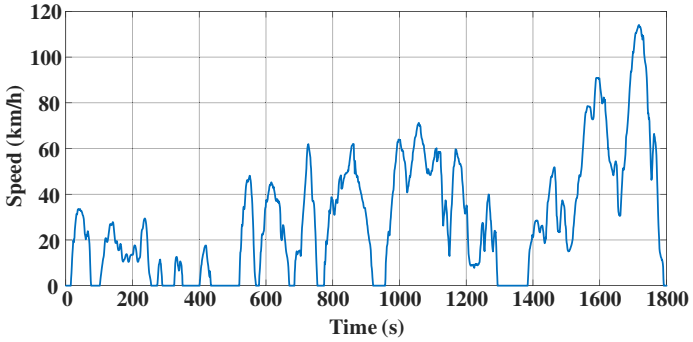

FIGURE 9. CLTC-P driving cycles.

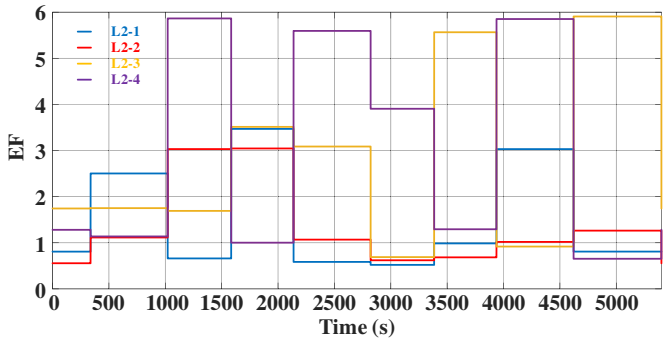

FIGURE 10. EFs of the level II optimization.

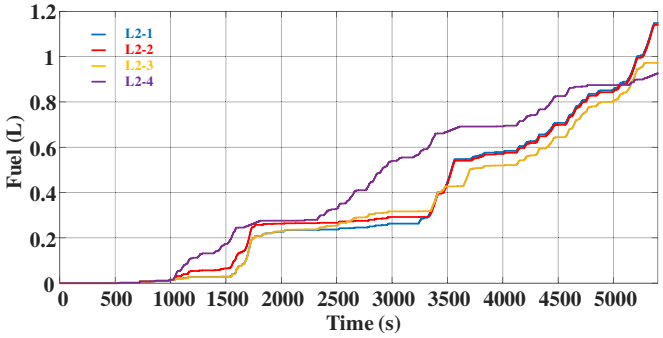

FIGURE 11. Fuel consumption of the level II optimization.

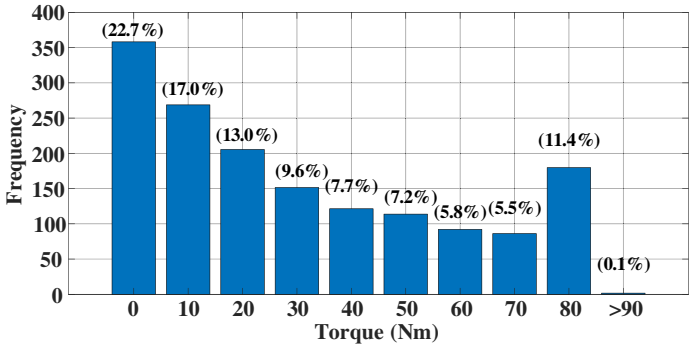

FIGURE 12. Frequency diagram of motor output torque under the CLTC-P.

TABLE 5. Results of the nested level optimization.

Point	Fuel consumption/L	Percentage change/%	SOC consumption/%
L2-1	1.15	23.66	4.91
L2-2	1.14	22.58	4.91
L2-3	0.97	4.30	4.99
L2-4	0.93	-	5.00

tion of EF values varies significantly across different operating regions. For instance, vehicles equipped with the motor corresponding to candidate point L2-1 consistently adopt small to medium EF values throughout the entire cycle, whereas those with L2-3 and L2-4 motors are optimized to achieve EF values of approximately 6 in different phases. Regarding the primary objective of minimizing fuel consumption, it can be observed from Fig. 11 that point L2-4 exhibits the lowest fuel consumption. Fig. 12 shows the frequency diagram of motor output torque under the CLTC-P. Combining the characteristic that the motor in the HEV is primarily responsible for low-speed starting with Fig. 12, it can be seen that under the CLTC-P driving cycle, the motor's operating points are mainly concentrated between 0 and 30 Nm, accounting for 30% of the total. Moreover, operating points below 55 Nm constitute 77.2% of the total. As shown in Fig. 11, within the low-torque range, the motor corresponding to points L2-4 exhibits higher efficiency. Therefore, under the same engine conditions, this motor demonstrates better economic potential, and it was selected as the final optimal solution in this study. Other detailed results are presented in Table 5. The lowest fuel consumption was achieved by the L2-4 solution at 0.93 L, which saved 23.66% compared to the L2-1 solution with the highest consumption. In addition, the battery state of charge (SOC) consumption remained almost identical across all four motors.

5. CONCLUSION

In this paper, a nested-level optimization for PMSM applied in HEVs has been presented. Compared with other optimization methods, the proposed one has the following advantages.

(1) The Morris sensitivity analysis is employed to identify the parameters to be optimized, and hierarchical optimization is used to reduce complexity and dimensions.

(2) The Kriging model and NSGA III algorithm are employed to reduce the computational cost of finite element analysis and to quickly solve the Pareto front.

(3) The nested optimization architecture integrates motor structure optimization with vehicle energy management optimization, enabling the attainment of a solution that is more suitable for the vehicle and its driving cycles on the Pareto front. The results show that the final motor rotor structure obtained using this architecture can save up to 23.66% of fuel consumption compared to other high-performance points on the Pareto front.

ACKNOWLEDGEMENT

This work was supported by the National Natural Science Foundation of China (Grant No. 52402449) and the Natural Sci-

ence Foundation of the Jiangsu Higher Education Institutions of China (Grant No. 1020241096).

REFERENCES

[1] Liang, C., H. Sun, X. Xu, F. Wang, and Z. Zhou, "PCE-based uncertain PWA modeling and control for DMHP mode transition system," *ISA Transactions*, Vol. 167, 2030–2045, 2025.

[2] Shimizu, Y., "Automatic design system with generative adversarial network and vision transformer for efficiency optimization of interior permanent magnet synchronous motor," *IEEE Transactions on Industrial Electronics*, Vol. 71, No. 11, 14 600–14 609, 2024.

[3] Soomro, A. H., "Design and analysis of interior permanent magnet motor for hybrid electric vehicles," *International Journal of Electrical Engineering & Emerging Technology*, Vol. 6, No. 1, 44–52, 2023.

[4] Liang, C., X. Xu, D. J. Auger, F. Wang, and Z. Zhou, "Optimized coordinated control strategy for dual motor hybrid powertrain with actuator response hysteresis: Minimizing effects of network-induced delays," *IEEE Transactions on Transportation Electrification*, Vol. 11, No. 5, 10 873–10 885, 2025.

[5] Sun, X., Z. Shi, G. Lei, Y. Guo, and J. Zhu, "Multi-objective design optimization of an IPMSM based on multilevel strategy," *IEEE Transactions on Industrial Electronics*, Vol. 68, No. 1, 139–148, 2021.

[6] Im, S.-Y., K.-S. Cha, Y.-J. Won, Y.-Y. Choi, and M.-S. Lim, "Two-step optimum design process of PMSM to improve driving efficiency and harmonics of lightweight electric vehicle," *IEEE Transactions on Industry Applications*, Vol. 59, No. 6, 6685–6694, 2023.

[7] Zhao, J., Y. Ding, Y. Wang, L. Deng, L. Yang, X. Liu, and W. He, "Design and optimization of a slotless PMSM with hexagon distributed FPCB winding," *IEEE Transactions on Industry Applications*, 1–10, 2025.

[8] Serat, Z., M. Danishmal, and F. M. Mohammadi, "Optimizing hybrid PV/Wind and grid systems for sustainable energy solutions at the university campus: Economic, environmental, and sensitivity analysis," *Energy Conversion and Management: X*, Vol. 24, 100691, 2024.

[9] Guan, D., X. Cong, J. Li, P. Wang, Z. Yang, and X. Jing, "Theoretical modeling and optimal matching on the damping property of mechatronic shock absorber with low speed and heavy load capacity," *Journal of Sound and Vibration*, Vol. 535, 117113, 2022.

[10] Yu, Y., Y. Pan, Q. Chen, Y. Hu, J. Gao, Z. Zhao, S. Niu, and S. Zhou, "Multi-objective optimization strategy for permanent magnet synchronous motor based on combined surrogate model and optimization algorithm," *Energies*, Vol. 16, No. 4, 1630, 2023.

[11] Pan, Z., S. Fang, H. Wang, and Y. Zhong, "Accurate and efficient surrogate model-assisted optimal design of flux reversal permanent magnet arc motor," *IEEE Transactions on Industrial Electronics*, Vol. 70, No. 9, 9312–9325, 2023.

[12] Das, S., A. Chowdhury, Y. Sozer, M. B. Kouhshahi, A. P. Ortega, Z. Wan, and J. Klass, "Sensitivity analysis based NVH optimization in permanent magnet synchronous machines using lumped unit force response," *IEEE Transactions on Industry Applications*, Vol. 58, No. 3, 3533–3544, 2022.

[13] Liu, L., Y. Guo, W. Yin, G. Lei, X. Sun, and J. Zhu, "Efficient design optimization of PMSM drive systems using improved equivalent-circuit-based loss minimization control," *IEEE Transactions on Industrial Electronics*, Vol. 72, No. 4, 3280–3291, 2025.

[14] Tan, D., Y. Wu, J. Lv, J. Li, X. Ou, Y. Meng, G. Lan, Y. Chen, and Z. Zhang, "Performance optimization of a diesel engine fueled with hydrogen/biodiesel with water addition based on the response surface methodology," *Energy*, Vol. 263, 125869, 2023.

[15] Jeong, Y.-J. and D.-K. Lim, "Optimal design of IPMSM using a surrogate model assisted effective sampling algorithm with kriging interpolation," *Journal of Electrical Engineering & Technology*, Vol. 20, No. 6, 4033–4046, 2025.

[16] Tahkola, M., V. Mukherjee, and J. Keränen, "Transient modeling of induction machine using artificial neural network surrogate models," *IEEE Transactions on Magnetics*, Vol. 58, No. 9, 1–4, 2022.

[17] Zhang, G. and T. Zhou, "Finite element model calibration with surrogate model-based bayesian updating: A case study of motor FEM model," *Innovations in Applied Engineering and Technology*, Vol. 3, No. 1, 1–13, 2024.

[18] Wang, Y., H. Zhang, J. Zhang, H. Yin, P. Wang, C. Zhang, and W. Hua, "Kriging-assisted multiobjective optimization of embedded magnetic encoder in PM synchronous machines," *IEEE Transactions on Instrumentation and Measurement*, Vol. 72, 1–12, 2023.

[19] Wang, J., Y. Hua, B. Xu, and Y. Zhu, "Multi-objective optimization design of bearingless interior permanent magnet synchronous motor based on MOWOA," *Electronics*, Vol. 14, No. 15, 3080, 2025.

[20] Shimizu, Y., S. Morimoto, M. Sanada, and Y. Inoue, "Automatic design system with generative adversarial network and convolutional neural network for optimization design of interior permanent magnet synchronous motor," *IEEE Transactions on Energy Conversion*, Vol. 38, No. 1, 724–734, 2023.

[21] Yi, C., H. Hofmann, and B. I. Epureanu, "Design and control co-optimization of a mixed hybrid electric powertrain architecture," *SAE International Journal of Electrified Vehicles*, Vol. 12, No. 2, 185–200, 2023.

[22] Mostashiri, A. and M. Montazeri-Gh, "Hybrid reinforcement learning optimization of aging aware energy management and powertrain sizing in fuel cell hybrid electric vehicles," *Scientific Reports*, Vol. 16, 4166, 2026.

[23] Kim, D.-M., S.-G. Lee, D.-K. Kim, M.-R. Park, and M.-S. Lim, "Sizing and optimization process of hybrid electric propulsion system for heavy-duty vehicle based on gaussian process modeling considering traction motor characteristics," *Renewable and Sustainable Energy Reviews*, Vol. 161, 112286, 2022.